Nanoscale

PAPER

View Article Online
View Journal | View Issue

Cite this: *Nanoscale*, 2026, **18**, 496

Cornea-SELEX-derived DNA aptamers for preparing spherical nucleic acids and corneal staining

Xiaohan Zhang,[a] Ka-Ying Wong,[a,b] Xinyuan Mu,[a] Qiushi Liu,[a] Xin Wang,[a] Man-Sau Wong [b,c,d] and Juewen Liu *[a,b]

Received 3rd November 2025,
Accepted 19th November 2025

DOI: 10.1039/d5nr04649a

rsc.li/nanoscale

Topical eye drops suffer from poor bioavailability due to rapid tear clearance and corneal barriers, which limit their therapeutic efficacy. Aptamers offer a promising solution for targeted ocular delivery and extended drug retention time. In this study, we employed gold nanoparticles (AuNPs) functionalized with aptamers previously selected to bind to porcine corneal tissues, forming spherical nucleic acids (SNAs). The binding of the SNAs to corneal tissues and human corneal epithelial cells (HCECs) was investigated. A total of six different aptamers were tested, each with an extended poly-adenine tail to attach to AuNPs using the thermal evaporation method. Among the six SNAs, the one prepared using the Cornea-S5 aptamer exhibited the best colloidal stability and optimal binding to both corneal tissues and HCECs, and it can specifically stain scarred regions. Flow cytometry determined the dissociation constant of Cornea-S5 to HCECs to be 169 nM. These findings highlight the potential of aptamer–AuNP conjugates for precise ocular drug delivery and diagnostics.

Introduction

Topical eye drops are the most commonly used treatment for a wide range of ocular diseases, from dry eye syndrome to infections.[1] However, their therapeutic efficacy is limited by rapid elimination due to blinking and tear drainage, necessitating frequent administration throughout the day.[2] The ocular surface presents several physiological and anatomical barriers, including rapid tear turnover (within 1–2 minutes), tight corneal epithelial junctions, enzymatic degradation, and nasolacrimal drainage.[3] These factors result in poor drug bioavailability, typically less than 5%, which contributes to suboptimal treatment outcomes, low patient compliance, and potential systemic side effects.[4] To overcome these limitations, various drug delivery systems based on both natural and synthetic polymers have been explored.[5–7] Natural polymers such as chitosan and hyaluronic acid offer mucoadhesive properties *via* electrostatic interactions with corneal mucins, thereby enhancing residence time.[8–11] Synthetic polymers like poly (lactic-*co*-glycolic acid) (PLGA) and polyethylene glycol (PEG) enable controlled drug release and degradation kinetics.[12–14]

Aptamers, single-stranded nucleic acids capable of high-affinity and selective binding to target molecules, represent another promising class of delivery agents.[15–17] Although aptamers have been developed against numerous targets,[18–20] only two aptamer-based drugs have gained FDA approval, both for ophthalmic indications. Notably, both pegaptanib (Macugen), approved in 2004, and avacincaptad pegol (Izervay), approved in 2023, function by inhibiting angiogenic growth factors implicated in age-related macular degeneration (AMD).[21,22] Beyond ligand binding, aptamers have been extensively investigated for cell-targeted drug delivery.[23–25] Despite their promise, clinical success remains limited compared to antibody-based systems. However, the eye presents a unique opportunity for localized, aptamer-mediated delivery. Unlike systemic administration, topical delivery to the ocular surface allows aptamers to avoid circulation-mediated clearance and protein fouling.

Nanomaterials are excellent vehicles for drug delivery.[26–30] Recent strategies have included conjugating mucin-binding aptamers to liposomes to enhance corneal adhesion.[31] A few other labs also used aptamer-conjugated materials for ocular drug delivery.[32,33] Our laboratory previously performed tissue-SELEX (systematic evolution of ligands by exponential enrichment) using porcine corneal tissue and identified several aptamers with moderate affinity (K_d ~300 nM) to human corneal epithelial cells.[33] Fluorescently labeled liposomes conjugated

[a]*Department of Chemistry, Waterloo Institute for Nanotechnology, University of Waterloo, Waterloo, ON N2L 3G1, Canada. E-mail: liujw@uwaterloo.ca*
[b]*Centre for Eye and Vision Research (CEVR), 17 W Hong Kong Science Park, Hong Kong, China*
[c]*Department of Food Science and Nutrition, The Hong Kong Polytechnic University, Hung Hom, Kowloon, Hong Kong, China*
[d]*Research Center for Chinese Medicine Innovation, The Hong Kong Polytechnic University, Hung Hom, Kowloon, Hong Kong, China*

with these aptamers adhered to corneal tissues, although their spatial distribution varied, likely due to the multi-layered corneal structure involved in aptamer selection. In our previous study, we focused on the top two most abundant aptamers from our SELEX, but we have obtained many families of aptamers, and some might have even stronger binding affinities. In the present study, we systematically investigate the binding characteristics of six of these aptamers using AuNPs, which serve both as imaging agents due to their high optical extinction coefficients and as size-relevant models for drug carriers.[34] By comparing six AuNP–aptamer conjugates, also known as SNAs,[35,36] we observed distinct binding and aggregation patterns on corneal tissues and cells, shedding light on the aptamers' differential affinities and potential for targeted ocular delivery. The SNAs appeared to concentrate on ocular surface injury sites and might serve as a stain to indicate such damage.

Materials and methods

Chemicals

Pig eyeballs were purchased from a local supermarket (Highland Packers Ltd, Stoney Creek, Ontario). The cornea–sclera tissues were excised using dissecting scissors, and 5 mm corneal discs were obtained with a biopsy punch. $HAuCl_4$ was purchased from Sigma-Aldrich. All DNA samples were obtained from Integrated DNA Technologies Inc. (Coralville, IA, USA). Acrylamide, *N*-isopropylacrylamide (NIPAm), *N*,*N*′-methylenebis(acrylamide) (BIS), sodium dodecyl sulfate (SDS), ammonium persulfate (APS) and *N*,*N*,*N*′,*N*′-tetramethylethylenediamine (TEMED) were from VWR. All other buffers and solutions were prepared using ultrapure water (>18.25 MΩ, Millipore). The absorption spectra were measured using an Agilent 8453 UV-vis spectrometer. Thermal drying was performed in a dry bath with a metal block (Eppendorf Thermomixer F1.5).

Preparation of AuNPs

AuNPs were prepared using the sodium citrate reduction method as previously reported.[37] Briefly, all glassware was soaked overnight in aqua regia (HNO_3 : HCl = 1 : 3), followed by rinsing with ultrapure water. To prepare 13 nm AuNPs, 100 mL of 1 mM $HAuCl_4$ solution was added to a 250 mL flask and then heated to boiling. Subsequently, 10 mL of 38.8 mM sodium citrate solution was added quickly with stirring, which resulted in a color change of the solution from pale yellow to wine red in 20 min. After cooling down to room temperature, the prepared 13 nm diameter AuNP solution was stored at 4 °C in the dark until further use.

Preparation of DNA-functionalized AuNPs by thermal drying

The preparation of SNA followed the method reported by our group.[38] Briefly, an AuNP solution (500 μL, 10 nM) was centrifuged at 13 000 rpm (≈14 200*g*, Eppendorf 5424, FA-45-24-11 rotor) for 15 min, and ~495 μL of the supernatant was discarded to concentrate the AuNPs by 100-fold. Then, an appropriate molar ratio of DNA was added (in most experiments, 10 μL of 100 μM A_5T_8 DNA and 1 μL of 1 mM A_3T_2 DNA) to reach a final DNA ratio of 1 : 1. The resulting solution was evaporated to dryness on a dry bath at 90 °C, taken out immediately after drying (drying time approximately 12 min), and redissolved with water to an appropriate volume (typically 500 μL). When necessary, the product was briefly sonicated for a better redispersion in water. After that, the AuNPs were washed three times by centrifugation to remove excess DNA and resuspended in 0.01 M PBS buffer until use.

TEM

The size and shape of the SNAs were characterized using a Hitachi HT7800 transmission electron microscope (TEM). A 20 μL aliquot of SNA-S5 was dropped onto an ultrathin carbon-coated copper grid and allowed to stand for 20 min at room temperature. After incubation, the excess solution was carefully removed, and the grid was subsequently air-dried for 24 h at room temperature.

HCEC cell culture and viability test

HPV-immortalized HCECs (a gift from Dr M. Gorbet at the University of Waterloo) were cultured using the following procedures. The cells (passages 6–10) were maintained in DMEM/F12 medium supplemented with 1% FBS and 1% penicillin/streptomycin at 37 °C, 95% humidity, and 5% CO_2. The cell medium was changed every 3 days. HCECs were incubated with SNAs at a concentration of 10 nM for 2 hours, and cell viability was assessed using the AlamarBlue assay.

Preparation of hydrogels

To prepare polyacrylamide hydrogels, a 30% stock solution was prepared by dissolving acrylamide and bis-acrylamide (15 : 1) in buffer A (20 mM HEPES, pH 7.5, 4% glycerol). Then, 1 mL of the stock solution was purged with N_2 for 30 min to remove the dissolved oxygen. After that, 20 μL of 60 mg mL^{-1} SDS, 20 μL of 10% w/v APS and 0.6 μL TEMED were added successively. The mixture was added to a 96-well plate, and each well contained 100 μL solution. After gelation, the gels were collected for further use. To prepare agarose gels, agarose powder was dissolved in Milli-Q water to make a 3% solution and heated to 90 °C. After cooling to approximately 50 °C, the agarose solution was dispensed into a 96-well plate with each well containing 100 μL of solution for gelation.

Determination of dissociation constants

To investigate the binding affinity of FAM-labeled aptamers to the cells, HCECs were harvested using a scraper. The cells were then incubated with blocking buffer (1% BSA, 0.1 mg mL^{-1} salmon sperm DNA in PBS) for 30 min at room temperature. After washing with PBS by centrifugation, 3×10^5 cells were incubated with pre-annealed Cornea-S5 aptamers at various concentrations in PBS for 30 min at room temperature. After incubation, the cells were rinsed three times with 500 μL of PBS and then resuspended in 200 μL of PBS. Fluorescence

signals were analyzed with a NovoCyte Flow Cytometer (Agilent Technologies). The equilibrium dissociation constant (K_d) value of each aptamer or aptamer liposome was obtained using GraphPad Prism 9.

Determination of endocytosis and optimal incubation time

HCECs were plated at 20 000 cells per well in a 96-well plate and were incubated with SNA5 for different time periods from 0.5 hours to 24 hours, followed by gentle washing with PBS twice to remove loosely bound particles. The cells were then fixed with 4% paraformaldehyde for 20 minutes and treated with 100 μM KCN for 10 minutes to selectively dissolve extracellular AuNPs.

Results and discussion

Cornea-SELEX-derived aptamers

Our group has recently performed aptamer selection using porcine cornea as the target tissue.[33] As illustrated in Fig. 1A, a 5 mm biopsy punch was used to extract tissue discs from the eyeballs. Although the intended target was the outermost layer of the excised cornea, the harvested tissue encompassed all anatomical layers of the cornea—epithelium, stroma, Descemet's membrane, and endothelium (Fig. 1B). From the aptamer selection process, the top six most abundant sequences, named Cornea-S1 to S6, are presented in Fig. 1C. These six sequences belong to six different families[33] and are likely to bind different surface molecules on the tissue. The predicted secondary structures of the six aptamers revealed distinct folding characteristics with different numbers and sizes of stem–loop motifs. Corean-S1 to S3 exhibited relatively simple hairpin-like structures with one or two small loops, suggesting higher rigidity and structural stability. In contrast, Cornea-S4 to S6 displayed more complex configurations containing multiple or larger loops, indicating greater conformational flexibility. Among them, Cornea-S5 features two well-defined asymmetric loops connected by stable stems, providing a balanced combination of stability and adaptability of the aptamer. Detailed 3D structures of the aptamers need to be solved using high-resolution structural biology methods such as NMR spectroscopy or X-ray crystallography.

In our previous studies, we primarily focused on the Cornea-S1 and Cornea-S2 aptamers, as they were the most enriched sequences in the final aptamer pool. The diversity of aptamers obtained might reflect the complex composition of the ocular surface, which includes various cell types and membrane-associated proteins. Notably, the tissue cross-sections used during selection represent disrupted cellular layers, with the upper surface corresponding to the epithelial region, the lower surface to the endothelium, and the lateral surface. However, distinguishing between these sides after sectioning remains challenging.

Spherical nucleic acids bind to the cornea

Due to the design of the SELEX library,[39,40] all six aptamers have a common feature of containing six to seven base pairs at the end. This feature made it easier to use the same method for bioconjugation to nanomaterials. While our previous work used liposomes to immobilize aptamers, we used AuNPs in this work. AuNPs possess exceptionally high extinction coefficients, making them ideal optical labels for visual

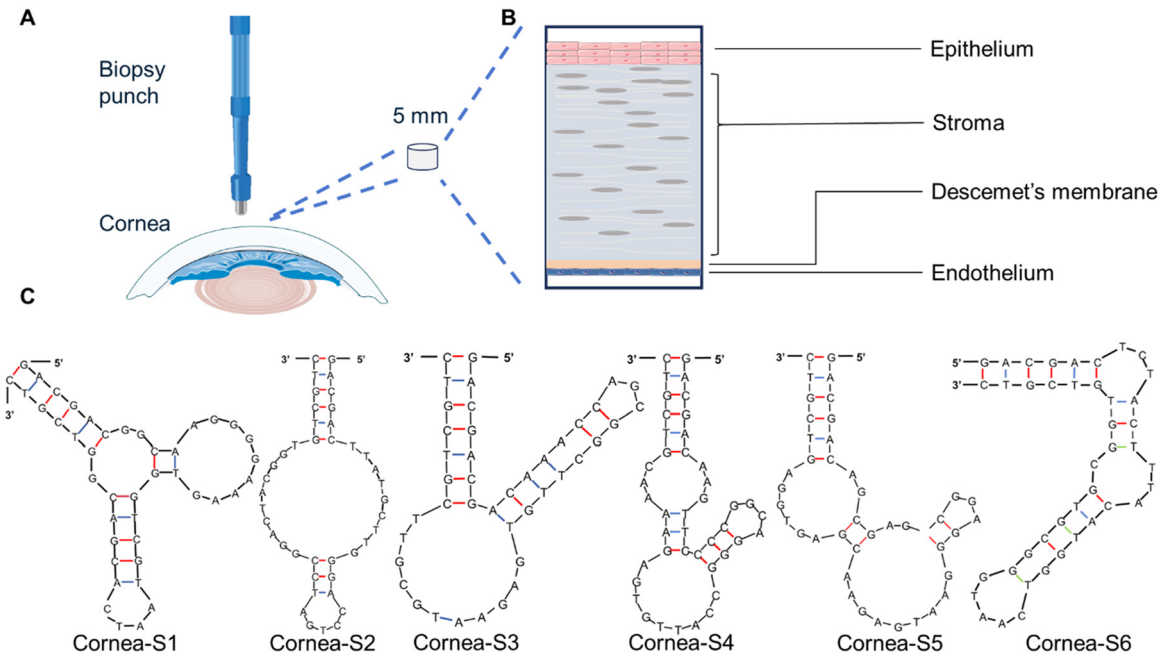

Fig. 1 (A) A schematic of the structure of the tissue sample used in our previous tissue-SELEX including different anatomical layers. (B) A schematic of the layered structure of the porcine cornea. (C) mFold-predicted secondary structures of the six aptamers used in this study.

detection.[41–43] When densely functionalized with DNA oligonucleotides, the formed SNAs have significantly enhanced cellular uptake, protection of DNA against nuclease degradation, and improved tissue penetration properties.[35,36,44–47] Since we need to test six aptamers, using more cost-effective non-thiolated aptamers for the functionalization of AuNPs is attractive. Various methods have been developed to achieve polyadenine-mediated attachment such as using salt,[48] pH,[49] and freezing.[50,51] However, they either have a low DNA density, low conjugate stability or poor sequence generality.[52] Our laboratory recently developed a thermal evaporation method to form stable SNAs with a very high density of non-thiolated DNA strands (Fig. 2A).[38] Using this technique, we designed aptamer sequences extended with a short thymine and adenine block (A_5T_8) to optimize their attachment to AuNPs (Fig. 2C).[53] To minimize steric hindrance from the long aptamer chains and to enhance colloidal stability, we introduced a short A_3T_2 sequence as a dilution strand. After the thermal evaporation treatment, the aptamers would attach to AuNPs *via* the A_5T_8 end. Based on dynamic light scattering (DLS), the average size of the SNAs slightly increased compared to the bare AuNPs from ~13 nm to ~17 nm. In addition, we also used TEM to confirm that aptamer functionalization did not alter the particle size or morphology of the AuNPs (Fig. S1).

We then optimized the ratio of the aptamer and the dilution strand. As shown in Fig. 2B, formulations with A_5T_8-aptamer: A_3T_2 ratios of 1 : 0.5 or 1 : 1 resulted in well-dispersed AuNPs with minimal aggregation. In contrast, higher proportions of A_3T_2 (ratios of 1 : 2 or 1 : 3) led to visible aggregation and a red shift in the UV-Vis absorbance peak to 560 nm. This is likely due to excessive surface coverage by the short A_3T_2 strands, limiting aptamer loading. Based on these results, we selected the 1 : 1 ratio for further experiments. The six prepared SNAs were named SNA1-6, respectively.

Staining the porcine cornea using the SNAs

The cornea–sclera tissues were excised using dissecting scissors, and 5 mm corneal discs were obtained with a biopsy punch (Fig. S2). To test the binding of the six SNA constructs, they were individually incubated with porcine corneal tissues for varying durations, followed by thorough washing with buffer and photographic documentation. All six SNAs demonstrated the ability to stain the tissue samples, whereas control experiments confirmed that these SNAs did not bind to non-biological hydrogels (Fig. S3 and S4), supporting their specific binding to the tissues. Upon closer inspection, distinct differences in color intensity and AuNP distribution were observed among the samples. To aid tissue orientation post-sectioning, the epithelial side of the cornea was stained with fluorescein and visualized under 470 nm blue LED excitation. Therefore, the fluorescence photographs shown in Fig. 3 all have the stained side oriented at the top. If unstained, no fluorescence could be observed (Fig. S2A).

Fluorescence and brightfield imaging revealed distinct accumulation patterns of the different SNAs on corneal tissues. Based on the images in Fig. 3A–C, SNA1, SNA2, and

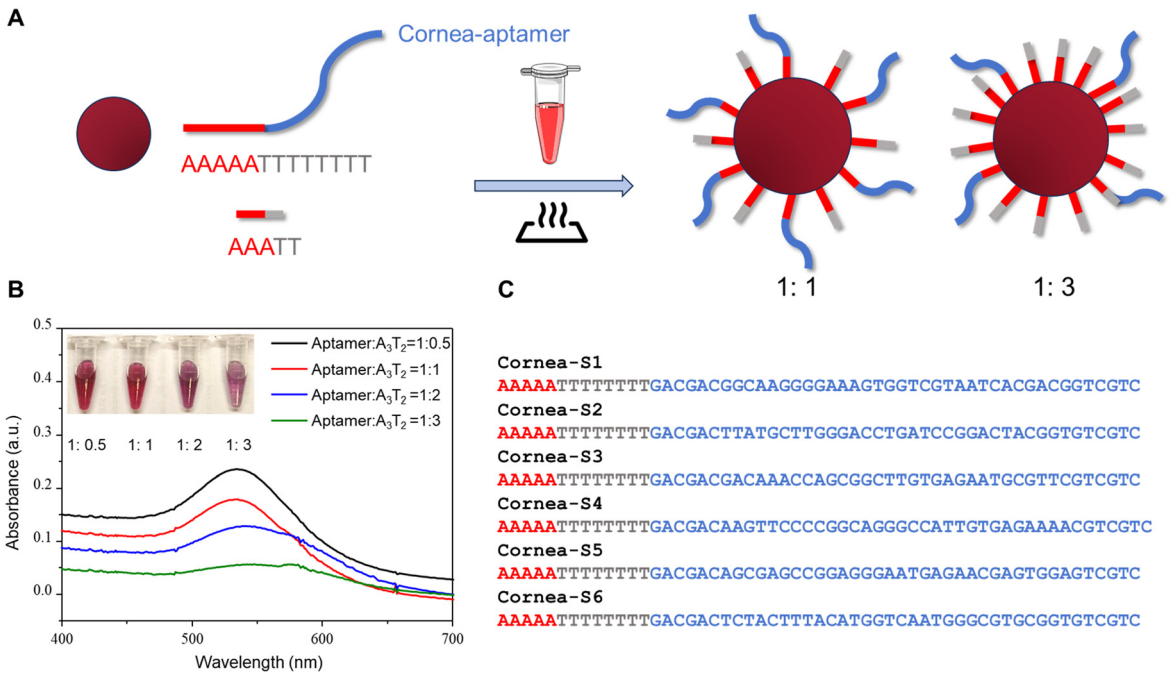

Fig. 2 (A) Schematic illustration of the thermal drying method for preparing non-thiolated SNAs and using a short A_3T_2 DNA to dilute the density of aptamers. Two ratios were shown to indicate the effect of the dilution strand on aptamer density. (B) UV-Vis spectra of different ratios of the A_5T_8-aptamer and A_3T_2 SNA-AuNPs, keeping the aptamer strand constant at 1 μM. (C) The six cornea-binding aptamers each have an A_5T_8 extension at the 5′-end.

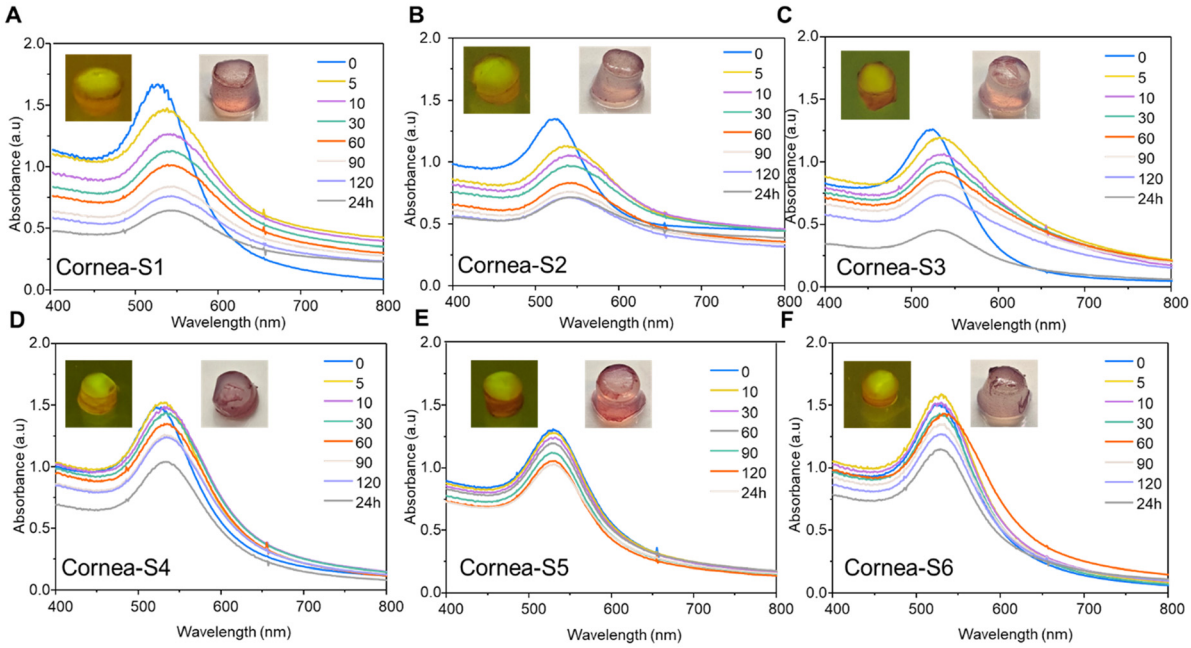

Fig. 3 UV-Vis spectra of the six SNAs incubated with a 5 mm cornea disc for different durations: (A) Cornea-S1, (B) Cornea-S2, (C) Cornea-S3, (D) Cornea-S4, (E) Cornea-S5, and (F) Cornea-S6. Fluorescence images were taken of cornea discs stained with fluorescein on the epithelial side of the cornea under 470 nm LED excitation.

SNA3 predominantly localized at the peripheral edges of the corneal discs, suggesting potential aggregation at these boundary regions. In contrast, SNA4 and SNA6 exhibited preferential localization to the lateral regions of the cornea, likely binding to the stromal layer (Fig. 3D and F). Notably, SNA5 showed a uniform distribution across the entire corneal surface (Fig. 3E), including both the central and peripheral regions, indicating effective and homogeneous surface interactions.

Time-dependent UV-Vis spectroscopy of the supernatants was employed to evaluate the adsorption behavior and colloidal stability of the SNAs upon exposure to corneal tissue. SNA1, SNA2, and SNA3 exhibited pronounced red shifts in their surface plasmon resonance peaks and significant reductions in absorbance intensity, indicating aggregation in the biological environment (Fig. 3A–C). SNA4 and SNA6 showed moderate spectral changes (Fig. 3D and F), reflecting partial aggregation or adsorption. In contrast, SNA5 demonstrated minimal spectral shift and the least reduction in absorbance over time, suggesting superior colloidal stability and minimal aggregation (Fig. 3E). These findings highlight SNA5 as the most promising aptamer candidate for forming stable SNAs and achieving uniform interaction with the corneal surface.

Effects of SNAs on cultured human corneal epithelial cells

After studying the interactions between the SNAs and corneal tissues, we further evaluated the interactions between the SNAs and HCECs. We cultured a batch of HCEC lines for *in vitro* testing (Fig. 4A). Initially, unwashed cells were observed to be covered with aggregated SNAs (the black dots in Fig. S5). Thus, washing steps were performed to evaluate the binding of SNAs to HCECs. To serve as a negative control, an SNA with a random sequence but of identical length to the aptamers was designed and conjugated to AuNPs, and cells incubated with this control SNA did not retain much of the AuNPs after washing (Fig. 4B).

In contrast, SNAs constructed with Cornea-S1–S4 aptamers exhibited moderate retention in HCECs post-washing (Fig. 4C–F), although significant aggregation was still noted, as reflected in the larger apparent particle sizes. The most favorable results were obtained for SNA-Cornea-S5 and SNA-Cornea-S6 (Fig. 4G and H), which showed minimal aggregation and uniformly distributed nanoparticles with smaller sizes (smaller black dots). Observation under a 40× biological inverted microscope confirmed that both Cornea-S5 and Cornea-S6 yielded a high density of well-dispersed AuNPs on the HCEC surface, suggesting superior binding affinity and cellular interaction. These findings underscore the strong targeting capabilities of Cornea-S5 and Cornea-S6 aptamers toward HCECs, and the observations were consistent with the photograph results shown in Fig. 3.

Binding kinetic experiments on HCEC cells

To understand whether the SNAs were adsorbed onto the cell surface or internalized by HCECs and to assess the kinetics of internalization, additional localization experiments were performed. We took advantage of AuNP dissolution by KCN.[54] If AuNPs are internalized by cells, they can be protected by the cell membrane and retain their integrity. If only adsorbed, AuNPs would be dissolved by KCN. For this experiment, HCECs were incubated with 10 nM SNA5 for varying durations

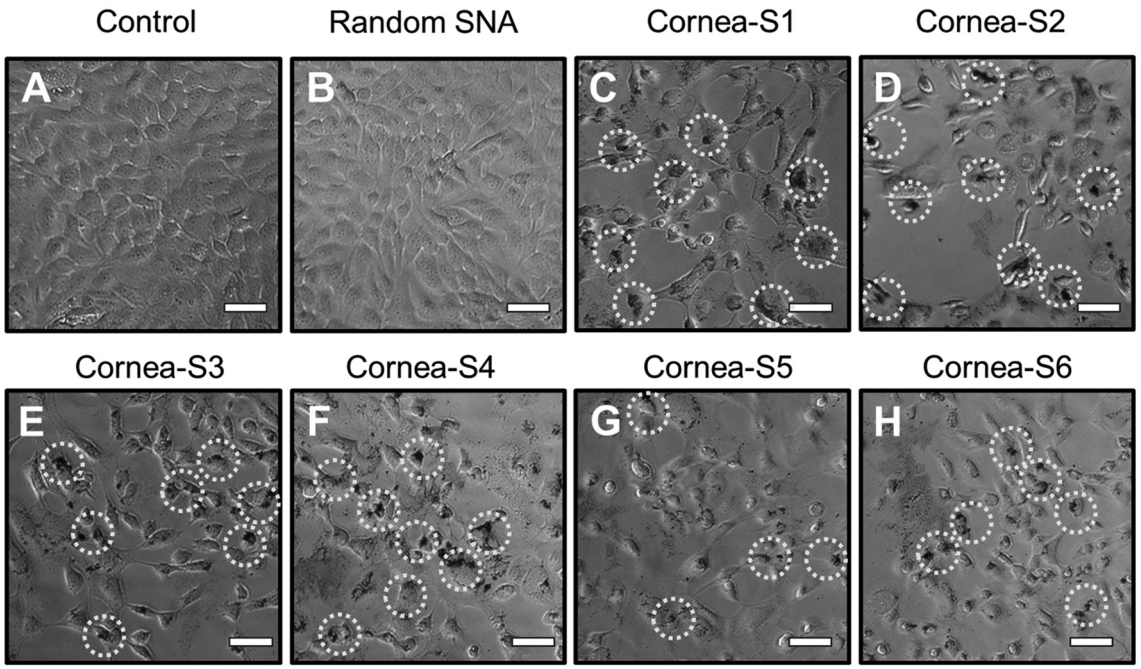

Fig. 4 Micrographs of HCEC cells after incubation with cornea aptamer SNAs of different sequences and a random sequence: (A) normal cells without treatment, (B) random-sequence SNA, (C) Cornea-S1 SNA, (D) Cornea-S2 SNA, (E) Cornea-S3 SNA, (F) Cornea-S4 SNA, (G) Cornea-S5 SNA, and (H) Cornea-S6 SNA. SNAs were washed with PBS buffer before imaging. Scale bars: 50 μm. Aggregated SNAs are indicated by the white circles, and the least aggregation was seen in Cornea-S5 SNA.

(0.5–24 h), and the cells were then gently washed with PBS twice and then fixed with 4% paraformaldehyde for 20 min before adding 100 μM KCN for 10 min (Fig. 5A–F). No obvious AuNP feature was observed within 1 h. At 2 h, distinct intracellular localization appeared, indicating effective uptake. Prolonged incubation (≥4 h) resulted in the internalization of

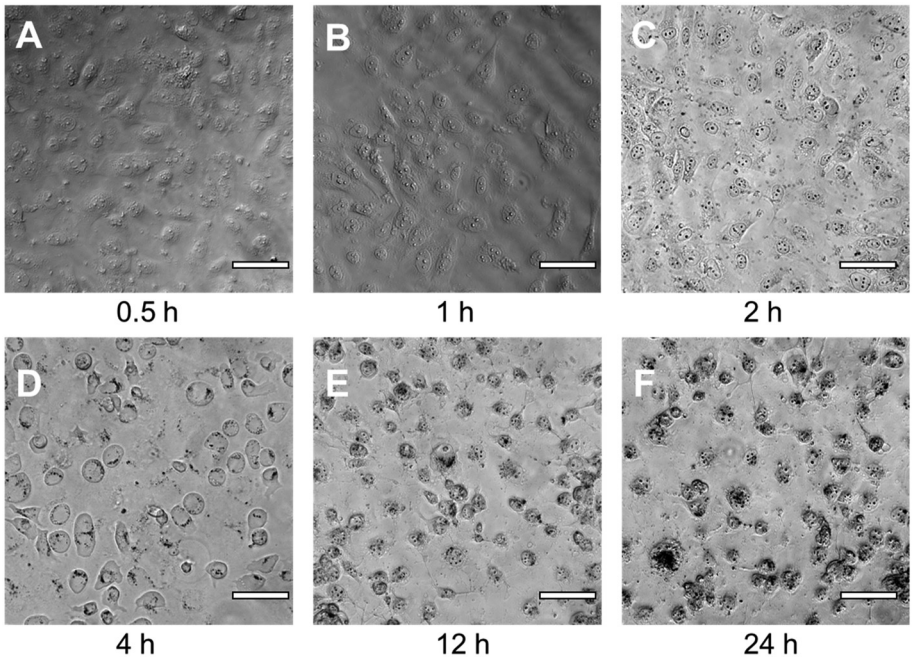

Fig. 5 Microscope images of HCEC cells with Cornea S5 SNA for different incubation times. KCN treatment after incubation of the SNA for (A) 0.5 h, (B) 1 h, (C) 2 h, (D) 4 h, (E) 12 h, and (F) 24 h. Scale bar is 100 μm.

a large amount of AuNPs, which appeared to aggregate inside cells, likely due to accumulation in endosomes. Therefore, a 2 h incubation was selected as the optimal condition for most of our experiments.

Aptamer binding assays

Based on the preceding results shown in Fig. 3, where the SNA with the Cornea-S5 aptamer stained the corneal surface evenly and did not aggregate much when incubated with HCECs, we selected the Cornea-S5 aptamer for further testing of its binding to HCECs, the outermost layer of the corneal surface. For comparison, Cornea-S1 and Cornea-S2 aptamers were included as control groups. To quantify binding affinity, we conducted flow cytometry and fluorescence microscopy experiments using carboxyfluorescein (FAM)-labeled aptamers (no AuNPs). To minimize nonspecific interactions, a blocking buffer was supplemented with bovine serum albumin (BSA) and salmon sperm DNA before incubation.

In our previous studies, the Cornea-S1 and Cornea-S2 aptamers demonstrated notable binding to HCECs, with K_d values of 362 nM and 174 nM, respectively.[33] In Fig. 6A and S6, flow cytometry analysis revealed that FAM-labeled Cornea-S5 has a K_d of 169 nM to HCECs, comparable to that of Cornea-S2, confirming its high binding affinity. Consistent with these findings, fluorescence microscopy showed green fluorescence corresponding to FAM-labeled aptamer binding and blue fluorescence marking cell nuclei (Fig. 6B). Among the three, Cornea-S1 exhibited the weakest fluorescence signal, while Cornea-S2 and Cornea-S5 produced more intense and uniform staining. These observations align with their measured K_d values and support the superior binding capability of the Cornea-S5 aptamer for HCECs.

Scar staining on porcine cornea

Given that we have obtained a cost-effective SNA that can stain the surface layers of the eye tissue, especially as they tend to stick to the edges of the excised corneal tissues, we wanted to test whether it can be used to stain ocular surface damage. To better simulate clinical application scenarios, we conducted *ex vivo* experiments using porcine cornea to assess the staining effects of SNAs. Fig. 7A and E show two corneal tissues that did not receive any treatment. To evaluate the binding efficiency of SNAs under injury conditions, we introduced corneal scarring by using a disposable razor blade (Fig. 7B and F). The regions containing the blade cut are indicated by boxes. In this experiment, we compared unmodified citrate-capped AuNPs with SNAs prepared using the Cornea-S5 aptamer. As shown in Fig. 7C, AuNPs without aptamer modification exhibited no observable staining in either scarred or intact regions of the corneal tissue. This lack of retention is attributed to the absence of specific affinity toward corneal cells. Following triple PBS washing, the majority of unmodified AuNPs were removed even after being treated with AuNPs for 12 hours (Fig. 7D).

In contrast, SNAs functionalized with Cornea-S5 showed prominent staining after just 10 minutes of incubation (Fig. 7G), with a substantial amount of AuNPs (visualized as pink coloration) retained on the corneal surface even after multiple PBS washes. Notably, after 12 hours of incubation at the same concentration, we observed significant enrichment of the AuNPs specifically within the scarred corneal region (Fig. 7H), indicating selective accumulation at the wound site. To further support the visual observation, we performed sectioning of the corneal tissues after SNA5 treatment and examined the samples using a biological inverted microscope.

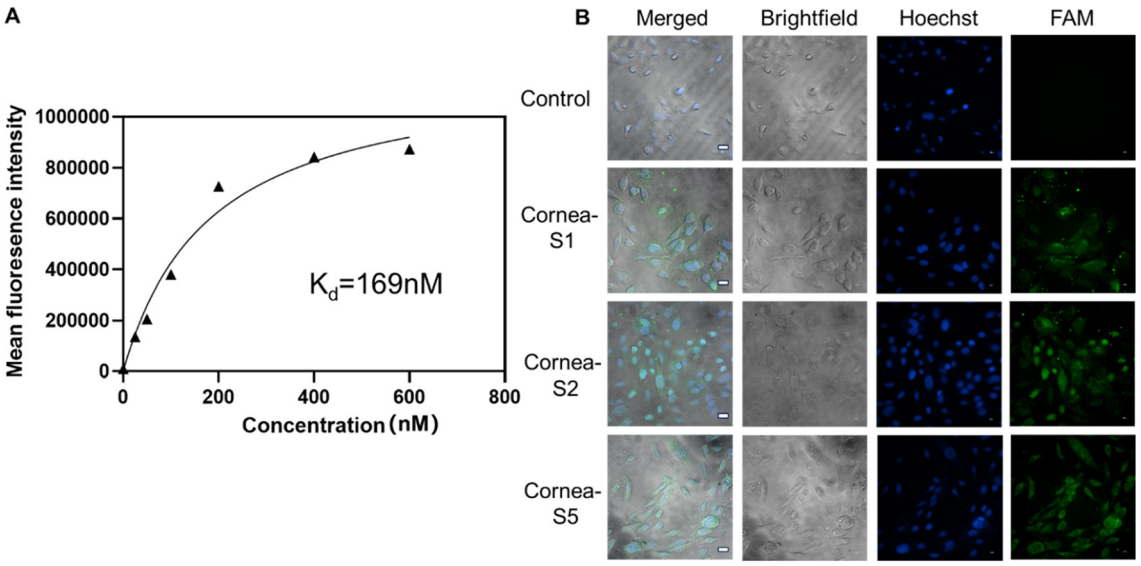

Fig. 6 Binding of the FAM-labeled Cornea-S5 aptamer to HCECs. (A) Dissociation constant (K_d) of Cornea-S5 to HCECs calculated based on flow cytometry. (B) Fluorescence micrographs showing the binding ability of FAM-labelled cornea aptamers to HCECs. The cell nuclei were stained with Hoechst to give blue nuclear fluorescence, and the green fluorescence was from FAM-labelled aptamers. Scale bars: 25 μm.

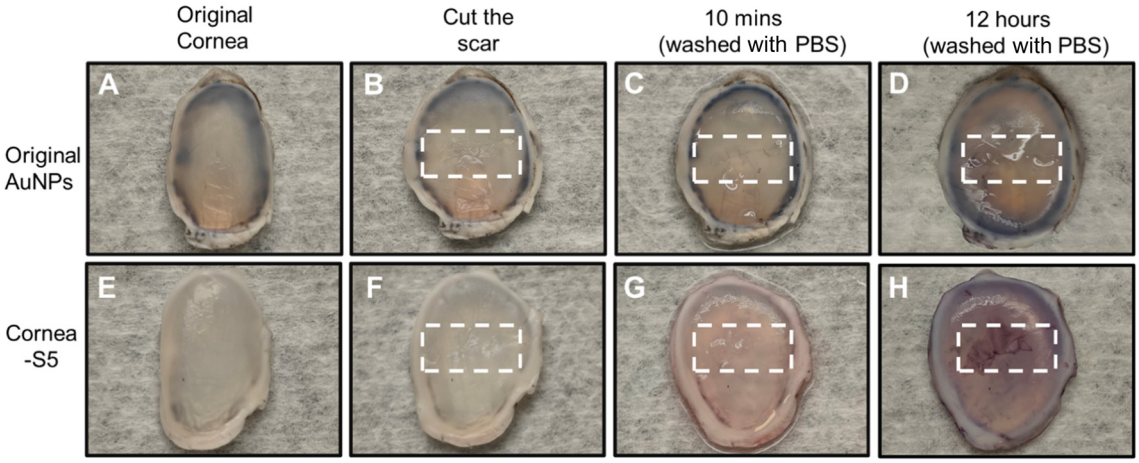

Fig. 7 Tissue samples treated with either unmodified AuNPs or SNA-Cornea-S5. For the unmodified AuNP group: (A) intact porcine cornea, (B) corneal scar region, (C) cornea incubated for 10 minutes with AuNPs and washed with PBS, and (D) cornea incubated for 12 hours with AuNPs and washed with PBS. For the SNA-Cornea-S5 treatment group: (E) intact porcine cornea, (F) corneal scar region, (G) cornea incubated for 10 minutes with SNA5 and washed with PBS, and (H) cornea incubated for 12 hours with SNA5 and washed with PBS. Scars approximately 3 mm in length were created on the corneal surface using a sterile scalpel. Equal concentrations of AuNP solutions were applied dropwise onto the corneas using a syringe. Following incubation, each sample was rinsed three times with PBS buffer.

Fig. S7A shows a region away from the incision site, where no apparent aggregation of SNAs was observed under bright-field microscopy. In contrast, Fig. S7B represents the cross-sectional view of the corneal wound area, as shown in the lower left image, where a clear and selective enrichment of gold nanoparticles can be seen at the wound surface. These results together provide direct visual evidence of the targeted accumulation of SNAs at the corneal injury site.

Finally, we performed cytotoxicity tests to evaluate the biocompatibility of aptamer-coated SNAs (S1–S6) as shown in Fig. S8. HCECs were incubated with SNAs at a concentration of 10 nM for 2 hours, and cell viability was assessed using the AlamarBlue assay. The results showed minimal cytotoxicity for all tested SNAs, with viability ranging from 92% to 97%, and no significant differences among the groups. These findings indicate that the SNAs exhibit excellent biocompatibility and are well-tolerated by HCECs.

Conclusion

This study presents a strategy for developing cornea-affinity SNAs through the screening of six aptamers derived from a previous cornea-SELEX experiment. These aptamers were extended to contain a poly-A tail and individually attached to AuNPs using the strong gold/adenine interactions. Based on the results derived from both visual observation and UV-Vis spectroscopic quantification, the Cornea-S5 SNA demonstrated superior binding affinity and colloidal stability. By optimizing the DNA sequence on AuNPs, this SNA achieved stable, non-aggregating SNAs capable of efficient tissue staining and cell targeting. Cornea-S5-SNA not only exhibited uniform distribution across the corneal surface but also demonstrated strong, selective binding to HCECs, as confirmed by fluorescence imaging and flow cytometry. Notably, the system distinguished scarred tissue from healthy tissue, highlighting its potential for diagnostic or therapeutic applications. The major advantage of this work lies in its integration of aptamer engineering with cost-effective SNA fabrication to achieve tissue-level targeting. Potential future applications include ocular drug delivery, injury localization, and intraoperative visualization.

Conflicts of interest

There are no conflicts to declare.

Data availability

The data that support the findings of this study are available from the Federated Research Data Repository at https://doi.org/10.20383/103.01506.

Supplementary information (SI) is available. See DOI: https://doi.org/10.1039/d5nr04649a.

Acknowledgements

Funding for this work was from the Natural Sciences and Engineering Research Council of Canada (NSERC), the Canada Research Chairs Program, and the InnoHK Initiative of the Innovation and Technology Commission of the Hong Kong Special Administrative Region Government. X. Zhang received a China Scholarship Council (CSC) postdoctoral scholarship to do research at the University of Waterloo.

References

1 A. C. Bisen, A. Dubey, S. Agrawal, A. Biswas, K. S. Rawat, S. Srivastava and R. S. Bhatta, *Ther. Delivery*, 2024, **15**, 463–480.
2 T. Loftsson, *Expert Opin. Drug Delivery*, 2022, **19**, 9–21.
3 M. H. Akhter, I. Ahmad, M. Y. Alshahrani, A. I. Al-Harbi, H. Khalilullah, O. Afzal, A. S. Altamimi, S. N. M. N. Ullah, A. Ojha and S. Karim, *Gels*, 2022, **8**, 82.
4 E. Batur, S. Özdemir, M. E. Durgun and Y. Özsoy, *Pharmaceuticals*, 2024, **17**, 511.
5 R. Cai, L. Zhang and H. Chi, *Front. Bioeng. Biotechnol.*, 2023, **11**, 1246974.
6 D. D. Nguyen and J.-Y. Lai, *Polym. Chem.*, 2020, **11**, 6988–7008.
7 T.-H. Tsung, Y.-C. Tsai, H.-P. Lee, Y.-H. Chen and D.-W. Lu, *Int. J. Mol. Sci.*, 2023, **24**, 12976.
8 V. Krishnaswami, R. Kandasamy, S. Alagarsamy, R. Palanisamy and S. Natesan, *Int. J. Biol. Macromol.*, 2018, **110**, 7–16.
9 P. Pahuja, S. Arora and P. Pawar, *Expert Opin. Drug Delivery*, 2012, **9**, 837–861.
10 M. Shao, Y. Chai, Y. Jiang, X. Wu, W. Xie, J. Lu, X. Fu, Y. He, X. Zhang and H. Zhang, *Adv. Mater.*, 2025, **37**, 2415353.
11 F. Yu, M. Zheng, A. Y. Zhang and Z. Han, *J. Controlled Release*, 2019, **315**, 40–54.
12 P. S. Chan, J. W. Xian, Q. Li, C. W. Chan, S. S. Leung and K. K. To, *AAPS J.*, 2019, **21**, 59.
13 J. J. López-Cano, A. Sigen, V. Andrés-Guerrero, H. Tai, I. Bravo-Osuna, I. T. Molina-Martínez, W. Wang and R. Herrero-Vanrell, *Pharmaceutics*, 2021, **13**, 234.
14 V. D. Wagh and D. U. Apar, *J. Nanotechnol.*, 2014, **2014**, 683153.
15 H.-M. Meng, T. Fu, X.-B. Zhang and W. Tan, *Natl. Sci. Rev.*, 2015, **2**, 71–84.
16 X. Wu, Y. Liu, D. Zhang, J. Yu, M. Zhang, S. Feng, L. Zhang, T. Fu, Y. Tan, T. Bing and W. Tan, *J. Am. Chem. Soc.*, 2024, **146**, 26667–26675.
17 K.-Y. Wong, M.-S. Wong, J. H. Lee and J. Liu, *Adv. Drug Delivery Rev.*, 2025, **224**, 115646.
18 H. Yu, O. Alkhamis, J. Canoura, Y. Liu and Y. Xiao, *Angew. Chem., Int. Ed.*, 2021, **60**, 16800–16823.
19 S. Kraemer, D. J. Schneider, C. Paterson, D. Perry, M. J. Westacott, Y. Hagar, E. Katilius, S. Lynch, T. M. Russell, T. Johnson, D. P. Astling, R. K. DeLisle, J. Cleveland, L. Gold, D. W. Drolet and N. Janjic, *J. Proteome Res.*, 2024, **23**, 4771–4788.
20 S. Stangherlin, N. Lui, J. H. Lee and J. Liu, *TrAC, Trends Anal. Chem.*, 2025, **191**, 118349.
21 C. Kang, *Drugs*, 2023, **83**, 1447–1453.
22 M. B. Sultan, D. Zhou, J. Loftus, T. Dombi, K. S. Ice and M. S. Group, *Ophthalmology*, 2011, **118**, 1107–1118.
23 J. R. Kanwar, K. Roy and R. K. Kanwar, *Crit. Rev. Biochem. Mol. Biol.*, 2011, **46**, 459–477.
24 X. Xie, F. Li, H. Zhang, Y. Lu, S. Lian, H. Lin, Y. Gao and L. Jia, *Eur. J. Pharm. Sci.*, 2016, **83**, 28–35.
25 N. Zhao, S.-N. Pei, J. Qi, Z. Zeng, S. P. Iyer, P. Lin, C.-H. Tung and Y. Zu, *Biomaterials*, 2015, **67**, 42–51.
26 M. J. Mitchell, M. M. Billingsley, R. M. Haley, M. E. Wechsler, N. A. Peppas and R. Langer, *Nat. Rev. Drug Discovery*, 2021, **20**, 101–124.
27 H. Han, S. Li, M. Xu, Y. Zhong, W. Fan, J. Xu, T. Zhou, J. Ji, J. Ye and K. Yao, *Adv. Drug Delivery Rev.*, 2023, **196**, 114770.
28 K.-Y. Wong, M.-S. Wong and J. Liu, *Adv. Healthcare Mater.*, 2025, **14**, 2401309.
29 K.-Y. Wong, Z. Nie, M.-S. Wong, Y. Wang and J. Liu, *Adv. Mater.*, 2024, **36**, 2404053.
30 M. Zandieh, J. H. Lee and J. W. Liu, *Chem. Sci.*, 2025, **16**, 14865–14883.
31 K.-Y. Wong, Y. Liu, L. Zhou, M.-S. Wong and J. Liu, *J. Mater. Chem. B*, 2023, **11**, 4684–4694.
32 K. G. Carrasquillo, J. A. Ricker, I. K. Rigas, J. W. Miller, E. S. Gragoudas and A. P. Adamis, *Invest. Ophthalmol. Visual Sci.*, 2003, **44**, 290–299.
33 K.-Y. Wong, Y. Liu, M. S. Wong and J. Liu, *Exploration*, 2023, **4**, 20230008.
34 K. Saha, S. S. Agasti, C. Kim, X. Li and V. M. Rotello, *Chem. Rev.*, 2012, **112**, 2739–2779.
35 J. I. Cutler, E. Auyeung and C. A. Mirkin, *J. Am. Chem. Soc.*, 2012, **134**, 1376–1391.
36 C. Xia, H. Cheng, X. Hou, Y. Zhang, X. Zhou, Q. Yan and S. Cao, *Adv. Sens. Energy Mater.*, 2024, **3**, 100117.
37 J. Liu and Y. Lu, *Nat. Protoc.*, 2006, **1**, 246–252.
38 X. Wang, Z. Yang, Z. Li, K. Huang, N. Cheng and J. Liu, *Angew. Chem., Int. Ed.*, 2024, **63**, e202410353.
39 L. Gu, H. Zhang, Y. Ding, Y. Zhang, D. Wang and J. Liu, *Smart Mol.*, 2023, **1**, e20230007.
40 K. Yang, N. M. Mitchell, S. Banerjee, Z. Cheng, S. Taylor, A. M. Kostic, I. Wong, S. Sajjath, Y. Zhang and J. Stevens, *Science*, 2023, **380**, 942–948.
41 R. Elghanian, J. J. Storhoff, R. C. Mucic, R. L. Letsinger and C. A. Mirkin, *Science*, 1997, **277**, 1078–1080.
42 G. B. Yao, J. Li, Q. Li, X. L. Chen, X. G. Liu, F. Wang, Z. B. Qu, Z. L. Ge, R. P. Narayanan, D. Williams, H. Pei, X. L. Zuo, L. H. Wang, H. Yan, B. Feringa and C. H. Fan, *Nat. Mater.*, 2020, **19**, 781–788.
43 H. Song, D. H. Jung, Y. Cho, H. H. Cho, V. G. Panferov, J. Liu, J. H. Heo and J. H. Lee, *Coord. Chem. Rev.*, 2025, **541**, 216835.
44 J. A. Dougan, C. Karlsson, W. E. Smith and D. Graham, *Nucleic Acids Res.*, 2007, **35**, 3668–3675.
45 D. A. Giljohann, D. S. Seferos, P. C. Patel, J. E. Millstone, N. L. Rosi and C. A. Mirkin, *Nano Lett.*, 2007, **7**, 3818–3821.
46 N. L. Rosi, D. A. Giljohann, C. S. Thaxton, A. K. R. Lytton-Jean, M. S. Han and C. A. Mirkin, *Science*, 2006, **312**, 1027–1030.
47 B. Liu and J. Liu, *Matter*, 2019, **1**, 825–847.
48 H. Pei, F. Li, Y. Wan, M. Wei, H. Liu, Y. Su, N. Chen, Q. Huang and C. Fan, *J. Am. Chem. Soc.*, 2012, **134**, 11876–11879.

49 X. Zhang, M. R. Servos and J. Liu, *J. Am. Chem. Soc.*, 2012, **134**, 7266–7269.
50 Y. Ding and J. Liu, *Chin. J. Chem.*, 2024, **42**, 2391–2400.
51 M. Hu, C. Yuan, T. Tian, X. Wang, J. Sun, E. Xiong and X. Zhou, *J. Am. Chem. Soc.*, 2020, **142**, 7506–7513.
52 X. Wang, S. Stangherlin, N. Cheng and J. Liu, *Adv. Sens. Energy Mater.*, 2025, **4**, 100132.
53 X. Wang, K. Huang, N. Cheng and J. Liu, *Biosens. Bioelectron.*, 2025, **289**, 117863.
54 F. Zhang, S. Wang and J. Liu, *Anal. Chem.*, 2019, **91**, 14743–14750.